WILEY-VCH

DOI: 10.1002/((please add manuscript number))
Article type: Communication

Colloidal Single-Layer Photocatalysts for Methanol-Storable Solar H_2 Fuel

Yingping Pang,[†] Md Nasir Uddin,[†] Wei Chen, Shaghraf Javaid, Emily Barker, Yunguo Li,[*] Alexandra Suvorova, Martin Saunders, Zongyou Yin,[*] and Guohua Jia[*]

Y. Pang, W. Chen, S. Javaid, E. Barker, Dr. G. Jia
Curtin Institute of Functional Molecules and Interfaces
School of Molecular and Life Sciences
Curtin University
Perth, WA 6845, Australia
E-mail: guohua.jia@curtin.edu.au

M. N. Uddin, Dr. Z. Yin
Research School of Chemistry
Australian National University
Canberra, ACT 2600, Australia
E-mail: zongyou.yin@anu.edu.au

Dr. Y. Li
Faculty of Mathematical and Physical Sciences,
University College London,
Gower Street, London WC1E 6BT, United Kingdom.
E-mail: yunguo.li@ucl.ac.uk

Dr. A. Suvorova, Prof. M. Saunders
Centre for Microscopy
Characterization and Analysis (CMCA)
The University of Western Australia
Perth, WA 6009, Australia

Keywords: single-layer transition metal dichalcogenides, two-dimensional materials, methanol-storable H_2 fuel, solar-driven photocatalysis

Molecular surfactants have been widely used to control morphologies of low dimension, including two-dimensional (2D) nanomaterials in colloidal chemical synthesis, but it is still highly challenging to accurately control single-layer growth for 2D materials. This work developed a scalable stacking-hinderable strategy to not only enable exclusive single-layer growth mode for transition metal dichalcogenides (TMDs) selectively sandwiched by surfactant molecules, but also retain sandwiched single-layer TMDs' photoredox activities. The single-layer growth mechanism was well explained by theoretical calculation. Three types of single-layer TMDs, including MoS_2, WS_2 and ReS_2, have been successfully synthesized and demonstrated in solar H_2 fuel production from hydrogen-stored liquid carrier -methanol. Such H_2 fuel production from single-layer MoS_2 is CO_x-free and reliably workable under room temperature and normal pressure with generation rate reaching ~ 617 μmole·g^{-1}·h^{-1} and excellent photoredox endurability. This strategy opens up the feasible avenue to develop methanol-storable solar H_2 fuel with facile chemical re-bonding actualized by 2D single-layer photocatalysts.

With continuous materials science advancing last decade, nano to atomic-thick 2D materials have been intensively studied from fundamental science, applied science to technological engineering, covering the areas of energy, environment, photonics, optoelectronic, electronics, biomedicine and sensing, etc.[1-3] Among these research activities, materials synthesis is, firstly, vitally important step no matter what applications to be targeted. Things normally go with two sides: when we want to thin/size down materials to pursue unique functionalities, more complicated synthesis protocols have to rely on, including the well-known surfactant directing strategy extensively used in colloidal synthesis. Colloidal chemistry has been playing vital roles and making huge contributions to our society and has become one of the most welcome synthesis methods for its ready upscalability towards

commercialization. Up to date, quite some 2D materials have been synthesized via colloidal chemistry, such as WS_2, CuS, MoS_2, $MoSe_2$, $MoTe_2$, TaS_2, SnS_2, InSe, TiS_2, ZrS_2, HfS_2, VS_2, NbS_2, TaS_2, $TiSe_2$, $ZrSe_3$, $HfSe_3$, VSe_2, $NbSe_2$, $TaSe_2$, GeS, GeSe, SnS_2, SnS, SnSe, Sb_2Te_3, Bi_2Te_3, CdS, CdSe, CdTe, ZnS, ZnSe, ZnTe, and PbS.[4-12] However, the functions from surfactants were mostly underestimated or even neglected; and regrettably, instead of being utilized, most surfactants will be removed by calcination to meet the requirements in various applications.

On the other hand, modern society is facing increasing energy exhaustion and deteriorating ecological environment issues due to the highly extensive usage of unsustainable sources like fossil fuels. Owing to its high energy density and zero pollution on environments, hydrogen energy, as the cleanest renewable energy carrier, holds great promise for green future. *In-situ* harnessing clean energy, hydrogen from aqueous-phase methanol at room temperature is a promising sustainable route towards "hydrogen economy" because methanol is rich hydrogen content (12.6 wt%), cheap and the easier manufacturing way from renewable resources,[13] which is expected to overcome the major obstacles coming from the physical properties of hydrogen so does for the transportation and handling issues.[14] However, the traditional catalytic fuel reforming processes, which are the major choices for hydrogen production over the years, liberate CO and/or CO_2 into the atmosphere along with their long demanding high temperatures (> 200 ^{o}C) and high pressure (25-50 bars) requirements. This limits its potential implementation in portable applications such as hydrogen vehicles.[13] To move away from above dilemma, an alternative approach could be the photocatalytic methanol decomposition into hydrogen and formaldehyde at room temperature as follows:[13]

$$CH_3OH \rightleftharpoons H_2 + CH_2O \qquad (1)$$

It is evident from reaction (1) that the photocatalytic methanol decomposition doesn't generate any CO_x compounds at all. Unfortunately, no work has reported solar-driven methano-to-H_2 fuel conversions at room temperature and normal pressure.[13,15]

Altavilla *et al.* reported a wet-chemical synthesis of single and multilayer MoS_2 nanosheets using oleylamine as the surfactant/solvent at a temperature as high as the boiling point of oleylamine, i.e. 360 ^oC.[16] Since this growth temperature for MoS_2 nanosheets is at the boiling point of the surfactant, oleylamine ligands are more prone to liberate from the surfaces of the nanomaterials, which in turn, leads to uncontrollable extensive stacking. Therefore, one of the main drawbacks of this synthesis is that the yield of single-layer MoS_2 nanosheets prepared at 360 ^oC is low as the layer-layer stacking will drive multilayer MoS_2 formation with increasing the reaction time, making it difficult to prepare high-yield single-layer MoS_2 nanosheets exclusively. Furthermore, the growth mechanism underpinning the formation of single-layer MoS_2 nanosheets is not yet known.

Herein, we demonstrated a scalable stacking-hinderable colloidal strategy to not only enable exclusive single-layer growth mode for transition metal dichalcogenides (TMDs) selectively sandwiched by surfactant molecules at a temperature of well below the boiling point of oleylamine, but also retain the photoredox activities from the sandwiched single-layer TMDs (Scheme 1). Our strategy is a general process that can be further expanded to synthesize other two types of high-quality single-layer TMDs such as WS_2 and ReS_2 nanosheets. Impressively, we first realized solar-driven recoverable methanol-to-pure hydrogen fuel conversion under room temperature and normal pressure using 2D single-layer photocatalysts (Scheme 1). Such H_2 fuel production is CO_x-free and reliably workable under room temperature and normal pressure with a generation rate reaching ~ 617 $\mu mole \cdot g^{-1} \cdot h^{-1}$ from single-layer MoS_2. The successful synthesis of single-layered TMDs in this work will put forward a new attempt for chasing efficient photocatalysts for high-efficiency methanol decomposition for hydrogen generation.

Single-layer MoS_2 anosheets were synthesized by a one-pot colloidal wet-chemical approach (see Methods for detailed information). The thermal decomposition of the single-source precursor of ammonium tetrathiomolybdate [$(NH_4)_2MoS_4$)] at 280 °C in the presence of octadecene (ODE) and oleylamine exclusively produced single-layer MoS_2 nanosheets (Figure 1a). Purification of the crude solution produced substantial amount of dried MoS_2 nanosheets, i.e. 1.26 g (Scheme 1) with a yield of >95% (Figure S1), which are about two orders of magnitude larger than the amount of nanoparticles obtained in a conventional colloidal synthesis. The low-magnification transmission electron microscopy (TEM) image (Figure S2) showed that the products were deposited on the amorphous carbon film. As shown in Figure 1a, roselike 2D MoS_2 nanosheets with distinct ripples and corrugations were clearly observed, demonstrating their ultrathin features. TEM measurements on nanosheets standing on their edges reveal a uniform thickness of ~0.6 nm (inset of Figure 1a), which is consistent with the thickness of the single-layer MoS_2 nanosheets.[17] Such single-layer nanosheets intertwined into a network structure owing to their ultrathin thickness. The atomic force microscopic (AFM) measurement further confirmed their uniform thickness of 0.6 nm corresponding to single-layer MoS_2 nanosheets (Figure 1b, Figure S3).

UV-Vis absorption spectroscopy was measured to correlate the optical properties to the number of layers of MoS_2 nanosheets (Figure 1c). The absorption spectra in Figure 1c reveals that the as-synthesized nanosheets have two absorption peaks at A (600 nm) and B (401 nm). These two absorption peaks can be attributed to the direct-gap transition between the maxima of split valence bands and the minimum of the conduction band located at the *K* point of the Brillouin zone. The absorption peak at 401 nm of the products is in good agreement with that of single-layer MoS_2 nanosheets and is significantly different from that of the three-layer (416 nm) and five-layer (424 nm) MoS_2 nanosheets.[18a] The as-prepared single-layer MoS_2 nanosheets could be easily re-dispersed in a variety of organic solvents ranging from chloroform, hexane to toluene for further use (inset of Figure 1c).

X-ray diffraction (XRD) measurement (Figure 1d) confirms the 2H phase of MoS_2 (JCPDS card no. 37-1492) of the products. Two obvious peaks at 33° and 56° can be indexed to the (100) and (110) planes of 2H MoS_2. A shoulder in the range of angles smaller than 30 degree in the XRD patterns corresponds to the organic oleylamine ligand, which has also been previously observed in other nanoparticles synthesized using oleylamine as the ligand.[18b,18c] The disappearance of the diffraction peak at 14.4° corresponding to the (002) lattice plane further proves the obtained products are single-layer MoS_2 nanosheets.[19,20] X-ray photoelectron spectroscopy (XPS) analysis was performed to explore the surface conditions and valence state of the single-layer MoS_2 nanosheets. The XPS survey spectrum shows that Mo and S elements coexisted in the system (Figure S4). The high-resolution XPS spectra show that the XPS spectrum of Mo_{3d} can be resolved into four peaks at around 235.4 eV, 232.5 eV, 232 eV and 229 eV, respectively (Figure 1e). The strongest peaks located at 232 eV and 229 eV can be assigned to Mo^{4+} $3d_{3/2}$ and Mo^{4+} $3d_{5/2}$, respectively.[21,22] As Mo^{4+} $3d_{3/2}$ and Mo^{4+} $3d_{5/2}$ of 1T phase MoS_2 show characteristic XPS peaks at 228.2 and 231.2 eV, the absence of these two peaks indicates that the prepared MoS_2 is 2H phase instead of 1T phase.[21] The peaks at 235.4 eV and 232.5 eV match well with the binding energy of Mo^{6+} 3d. The observed oxidation state of Mo may be attributed to presence of MoO_3 species, which is often observed in solution prepared MoS_2 nanosheets.[23] Two peaks (Figure 1f) located at 162.2 eV and 163.4 eV can be assigned to S $2p_{3/2}$ and S $2p_{1/2}$ of S(-2), respectively. The XPS results confirm the formation of the 2H phase MoS_2 nanosheets in terms of XPS peak positions and shapes for both Mo and S. The elemental mapping of MoS_2 nanosheets collected from high-angle annular dark-field (HAADF)-scanning TEM (STEM) reveals the homogeneous distribution of Mo (red) and S (green) through the whole nanosheets (Figure 1g-i). Both STEM-EDX mapping and EDX spectrum (Figure S5) further confirm the co-presence of both Mo and S in the obtained samples.

In this section, we will discuss how the thermal decomposition of single-source precursor of ammonium tetrathiomolybdate [$(NH_4)_2MoS_4$] produces single-layer MoS_2 nanosheets in the presence of oleylamine and ODE. Previous differential thermal analysis (DTA) and thermogravimetric analysis (TGA) indicate $(NH_4)_2MoS_4$ compound may decompose under vacuum by the following equation:[24]

$$(NH_4)_2MoS_4 \rightarrow MoS_2 + NH_3 + H_2S + S$$

Although the thermal decomposition of $(NH_4)_2MoS_4$ in oleylamine and ODE solutions could be very complex, the species formed in the reaction are similar to the products of the above equation. As MoS_2 has layered structures with relatively weak interlayer Van der Waals interactions, whether thermal decomposition of MoS_2 produces single-layer or multi-layer sheets will mostly likely depend on how strong of the adhesion energy among the MoS_2 layers in comparison to the adsorption energy of molecules binding on MoS_2.[25]

In this case, possible adsorbates are the NH_3 and H_2S molecules and the oleylamine surfactant. Since oleylamine exhibits affinity to surfaces through the $-NH_2$ functional group, one would expect a similar surface adsorption energy for both oleylamine and NH_3, which can be feasibly modelled by NH_3. We therefore investigated the effects of adsorbates on the interlayer cohesion of MoS_2 by comparing the interlayer cohesion strength of MoS_2 with the binding strengths of NH_3 and H_2S on the surfaces of MoS_2 (See Methods for details). The calculated E_{coh} are plotted in Figure 2b and 2c. The calculated adsorption energy per NH_3 molecule at a sparse occupancy of 25% (0.126 eV/molecule) agrees with previous data of 0.127 eV/molecule.[26] Nonetheless, no matter which functional is used, the binding of molecules with MoS_2 becomes stronger than the MoS_2 interlayer binding beyond ~55% occupancy (Figure 2b). Inset in Figure 2c shows the obtained most stable adsorption configurations for NH_3 and H_2S molecules on single-layer MoS_2 nanosheets. It should be noted that the obtained most stable configurations may not be the ground-state configurations, but for the ground state, the true adsorption energy should not be lower than the calculated

ones. As can be seen in Figure 2b and 2c, the interlayer cohesion is very weak for MoS_2, which can be surpassed by the adsorption of either NH_3 or H_2S molecules. In experiments we have an environment of mixed NH_3 and H_2S molecules. If the two types of adsorbed molecules are locally mixed on MoS_2 surface, it means that this is more energetically favorable than the situation where adsorbed NH_3 and H_2S molecules are locally separated as calculated above. Hence, the binding of molecules with MoS_2 in the presence of mixed molecules can only be further strengthened. Therefore, we attribute the exclusive formation of single-layer MoS_2 nanosheets to the effective and efficient interaction of adsorbate molecules between the MoS_2 interlayers. Such a scenario can be illustrated by the three-dimensional representation in Figure 2a.

The photocatalysts of single-layer MoS_2 nanosheets have been prepared using the surfactants like oleylamine, which have significant effects on the formation of single-layer MoS_2. To avoid any obvious questionable effects on H_2 production directly from the surfactants, between which the single-layer MoS_2 photocatalysts were sandwiched, we have tested the methanol to hydrogen (MTH) efficiency of the pure surfactant and mixture of methanol and surfactant (1:1, vol) solutions under control experimental conditions. It is found that the pure surfactant produces approximately 0.154 μmole of H_2 while the later one gives nearly 0.159 μmole of H_2. In terms of H_2 production rate, it represents nearly 0.0094 μmole g^{-1} h^{-1} while 2 mg of MoS_2 provides 617 μmole g^{-1} h^{-1}, as shown in the Figure 3a. This confirms that the preparation methods of single-layer MoS_2 nanosheets with surfactants don't have any effects on H_2 production from the surfactants themselves.

The concentration of MoS_2 nanosheets in methanol solution has significant effect on H_2 production as is seen from Figure 3b. The concentration profile shows that the H_2 production from methanol decomposition under solar light illumination follows an optimum condition and, in this case, it is 2 mg of MoS_2 samples in 10 mL methanol, i.e. 0.2 mg·mL^{-1}. We have tested three different amounts of samples and it is clearly evident that 2 mg of MoS_2 samples

give the highest production rate for H_2 among others. With increasing concentration from 0.1 mg·mL^{-1} to 0.2 mg·mL^{-1}, the H_2 amount was increased from 0.46 to 2.50 μmole followed a decline into 1.07 μmole. The plausible reason for that decrease is that the excess amount of MoS_2 nanosheets in the solution may hinder the photon availability into the active surface of catalysts. In the context of H_2 production rate, 2 mg of MoS_2 sample provides almost 617 μmole g^{-1}·h^{-1} after 2 h continuous solar irradiation, while the calculated values for 1 mg and 3 mg of MoS_2 samples are 229.30 and 178.03 μmole g^{-1}·h^{-1}, respectively as shown in Figure 3b.

For the practical application, both the cost of catalysts and their synthesis and the stability of catalyst performance are important. In this work, the metal dichalcogenides are composed from abundant elements and our developed one-step colloidal synthesis is low-cost up-scalable method. It deserves our effort to study the performance endurance of single-layer MoS_2's photoreaction. As seen from Figure 3c that the H_2 production was increased steadily over the course of light irradiation from 2.5 to 12.54 μmole followed by a steady state at 13.60 μmole for first cycle experiment. Correspondingly, the H_2 production rate after converting the unit tends to saturate with time (Figure S6). This pattern for H_2 production was maintained exactly the same in cycle two and three. The plausible reason for H_2 production reaching a steady state is that, first, the surface-active sites of single-layer MoS_2 nanosheets were covered by *in-situ* H_2 molecules and formaldehyde by-products, which kinetically limit the reactivity of MoS_2 with methanol molecules.[13] Under such conditions, the photoexcited electron-hole pairs on MoS_2 surface may easily recombine on the site resulting lower performance.[13] Second, with more and more H_2 molecules generated in a sealed reactor with constant volume, the up-building partial pressure from H_2 gases will suppress the forward methanol-to-hydrogen reaction, hence tending to a saturation phenomenon as observed in Figure 3c. What is significant is that the H_2 production rates are refreshable. After the photoreaction was stopped and opened the reactor to release the H_2 gases out of the reactor, we re-performed the same photoreaction using the same MoS_2 photocatalysts from cycle one

for the next cycle experiment. Surprisingly, the H_2 production rate can recover and reach the comparable level as last cycle, based on the rates of 617, 612, and 605 μmole g^{-1} h^{-1} for cycle one, two, and three, respectively, after first 2 h photoreaction as shown in Figure S6. That's to say the photocatalytic performance can be maintained at about 99% for the subsequent cycle. With excellent electronic and optoelectronic properties, single-layer MoS_2 nanosheets have been proven much stable under the operating conditions, at least for 198 h, which makes it potential to develop room-temperature and normal pressure liquid carrier for H_2 fuel with a sustainable way.

Figure 3d-i shows further characterizations of the photocatalytic materials after cycling. STEM and TEM images of the MoS_2 photocatalyst after cycling 198 h are shown in Figure 3d and 3g, respectively. After such long-time photocatalytic tests, we find the morphology of MoS_2 layers was preserved, and the elemental content of Mo and S were confirmed, as manifested by the STEM element mapping results (Figure 3e, 3f). The Mo 3d and S 2p binding energy (Figure 3h, 3i) in the samples after photocatalytic tests is in almost perfect agreement with that of single-layer MoS_2 nanosheets before the photocatalytic reaction. The above results overall demonstrate single-layer MoS_2, besides of high photocatalytic activity, also has good photocatalytic stability and durability in methanol dehydrogenation for hydrogen generation.

It is evident that the single-layer MoS_2 shows superior performance in terms of H_2 production, which is associated to its excellent photon harvesting, exciton generation and active photoredox reactions. Single-layer MoS_2 is a direct band-gap semiconductor with 1.8 eV energy gap and contains highly active edge sites, which is necessary for photocatalysis[27] and will be explored by theoretical calculation below.

We explored the catalytic hydrogen evolution reaction from methanol (CH_3OH) on the edges of single-layer MoS_2 nanosheets since the basal plane has been found chemically inert by both experimental and theoretical studies.[28-32] The edge structures were represented by a

semi-infinite MoS_2 stripe model as described in detail previously.[28,32] There can be two edge types, namely, the $(10\bar{1}0)$ Mo-edge and the $(\bar{1}010)$ S-edge. Two energetically favorable edge structures have been described before: the Mo-edge terminated with S monomers (denoted as Mo-edge-m) and the S-edge terminated with alternative S monomers and dimers (denoted as S-edge-m+d).[28,30,32] Here, we explored the catalytic hydrogen evolution on these two edges and another three edges: the Mo-edge without S termination (Mo-edge-b), the Mo-edge terminated with alternative S monomers and dimers (Mo-edge-m+d), and the S-edge terminated with S monomers (S-edge-m). The relaxed edge structures by using the PBE-D2 method are shown in Fig. 4a1-e1. The catalytic hydrogen evolution from methanol involves two key deprotonation reactions which are related to the O-H and C-H bond scissions. We considered the following pathway: the first process reaction is the adsorption of CH_3OH on edge sites of MoS_2 (denoted as *).

$$CH_3OH + * = CH_3OH * \qquad (P1)$$

and then it is the scission of O-H bond

$$CH_3OH * + * = CH_3O * + H * \qquad (P2)$$

or the scission of C-H bond

$$CH_3OH * + * = CH_2OH * + H * \qquad (P3)$$

These two processes above will be followed by

$$CH_3O * + * = CH_2O * + H * \qquad (P4)$$

and

$$CH_2OH * + * = CH_2O * + H * \qquad (P5)$$

respectively. The last stage will be the desorption of CH_2O, which can be represented by

$$CH_2O * = CH_2O + * \qquad (P6)$$

The reaction free energy ΔG can be expressed by

$$\Delta G = \Delta E + \Delta E_{ZPE} - T\Delta S$$

where ΔE, ΔE_{ZPE}, and ΔS are the potential energy difference, zero-point energy difference and change of entropy, respectively. Usually, ΔS is small and can be neglected. The correction due to ΔE_{ZPE} is normally less than 0.2 eV at 300 K, and considering ΔE_{ZPE} only further lowers ΔG for reactions above.[33] Therefore, we can just simply take $\Delta G \cong \Delta E$.

The calculated ΔG by using the PBE-D2 method for the elementary processes P1-P6 on the five edges are plotted in Fig. 4a2-e2. Of the five edges, we find the S-edge-m+d edge (Figure 4d2) is most favourable for deprotonation of methanol. The O-H bond scission (P2) is favoured over C-H bond scission (P3) for the first deprotonation of CH_3OH. The structures corresponding to P1, P2 and P4 occurred on the S-edge-m+d edge are plotted in Figure 4f1-f5.

It is postulated that the single-layer MoS_2 exposes active edge sites which is beneficial not only for the charge-carrier separation but also accelerates the reaction processes at the surface side and the improved photoactivity is ascribed to the excellent physical properties of MoS_2. The single-layer MoS_2 nanosheets has excellent electron mobility which is beneficial for effective charge carrier separation and transport across the active site. Upon light illumination, MoS_2 nanosheets produce photo-generated charge carriers while the holes on the valence band can easily oxidize the adsorbed CH_3OH to generate the methoxy radical intermediate, $CH_3O\bullet$ on MoS_2 edges (Figure S7). Due to their dynamical instability property, the intermediate were further oxidized into aldehyde (CHOH) (Figure S8). On the other hand, the photo-generated electrons at the conduction band of the MoS_2 reduces the protons into H_2 while leaving the aldehyde into the solution without any CO_x compounds, which nullifying the environmental pollution.

Importantly, our synthetic approach based on the decomposition of a single precursor is widely applicable. A series of nanocrystals of single-layer WS_2 and ReS_2 nanosheets were successfully synthesized. For example, when ammonium tetrathiomolybdate [$(NH_4)_2MoS_4$] was replaced by ammonium tetrathiotungstate [$(NH_4)_2WS_4$], single-layer WS_2 nanosheets with an average thickness of 0.6 nm (Figure 5a-c, Figure S9) were synthesized. The high-

resolution TEM image (Figure S10) shows that a lattice fringe of 0.309 nm, which corresponds to the (004) plane of WS_2 nanosheets. The diffraction peaks in the XRD pattern at 32.7° and 58.4° correspond to (100) and (110) planes of the 2H-WS_2 nanosheets, respectively (JCPDS card no. 08-0237) (Figure 5d). The XRD pattern of WS_2 nanosheets shows no crystal plane diffraction peak appearance at 14.4^o, indicating there is no stack along (002) plane, and thus proving the product is single-layer WS_2 nanosheets, which are in consistent with the results obtained from the TEM, STEM and AFM characterizations (Figure 5a-c). The UV-Vis absorption spectrum (Figure S11) does not show any obvious peak at 607 nm, which is in consistence with the previous results on single-layer WS_2 nanosheets.[34,35] The XPS survey scan (Figure S12), EDX spectrum (Figure S13) and STEM-EDX mapping (Figure S14) of the as-prepared nanosheets show W and S co-exist in the obtained nanosheets. Figure 5e and 5f show the high-resolution Mo 3d and S 2p XPS spectra of the single-layer WS_2 nanosheets. The characteristic W 4f energy peaks of the prepared single-layer WS_2 nanosheets are shown in Figure 5e. The presence of two characteristic peaks at 35.5 eV and 33.3 eV corresponding to $4f_{5/2}$ and W $4f_{7/2}$ of W^{4+}, respectively, confirm the formation of 2H-WS_2, as they are different from the characteristic peaks at 34 eV and 32 eV of 1T-WS_2. In addition, the XPS spectrum shows two weak peaks at ~36.3 eV and 39.2 eV, which can be assigned to the W-O species. The XPS peaks at 163.3 eV and 162.1 eV correspond to S $2p_{1/2}$ and S $2p_{3/2}$ respectively, of S (-2) (Figure 5f).[2]

Similarly, when single precursors such as tetrabutylammonium tetrathiorhenate(VII) [$(C_4H_9)_4$-$NReS_4$] were thermal decomposed in a solution of oleylamine and ODE, the single-layer ReS_2 nanosheets (Figure 5g-l, Figures S15-18) were also synthesized via the one-pot process, demonstrating the generality of this synthetic approach. Moreover, we have expanded this single-source precursor-based synthetic approach to prepare other non-layered materials such as Sn_2S nanosheets and Cu_xS nanoplates (Figure S19), which indeed further verifies the versatility of this synthetic route.

It is noteworthy that the hydrogen production from methanol over other single-layer WS_2 and ReS_2 also shows promise. It is found that the MTH efficiency for single-layer WS_2 is nearly 200 μmole $g^{-1}\cdot h^{-1}$ for 2 mg samples while single-layer ReS_2 contributes to about 130 μmole $g^{-1}\cdot h^{-1}$ for the same quantity of samples (Figure S20). We have verified that this excellent MTH efficiency solely comes from single-layer nanostructure necessarily sandwiched by the surfactants under performing the thermal annealing at 400 ^{o}C for MoS_2 catalysts. As seen from Figure S21, the higher the thermal exposure time, the more the H_2 production rate decreases. The rationale for this phenomenon is that upon thermal annealing, the surfactant will be partially or even fully removed. The coupling/stacking probability between the exposed single-layers will increase, which will transform MoS_2's single-layer structures into multilayer structures under the thermal treatment. Correspondingly, the physical property of semiconductor MoS_2 will also change; that's to say its direct bandgap nature from single-layer will be converted to indirect bandgap for multilayers.[36] Resultantly, the harvesting efficiency on solar photons, and hence the photoredox activity, will decrease as observed.

In summary, we reported a general scalable colloidal strategy to exclusively produce a family of single-layer TMD nanosheets from single-source precursors at a relatively low temperature. The intercalation of NH_3 and H_2S molecules between the layers weakens the interlayer attraction of TMDs, leading to the formation of single-layer TMD nanosheets. The single-layer photocatalysts demonstrated excellent photocatalytic performances in solar H_2 fuel production from hydrogen-stored liquid carrier–methanol with good stability and durability under room temperature and normal pressure. This work provides a basis for methanol-storable solar H_2 fuel production using 2D single-layer photocatalysts.

Experimental Section

Synthesis of single-layer TMDs nanosheets

Synthesis of single-layer MoS_2 nanosheets: In a typical synthesis of single-layer MoS_2 nanosheets, ammonium tetrathiomolybdate [$(NH_4)_2MoS_4$, 4 mmol] was mixed with 7 mL of oleylamine and 8 mL of ODE in a 50 mL three neck round bottom flask. The mixture was degassed at 110 °C for 30 min. Then, the temperature was raised to 280 °C under N_2 flow, and kept at this temperature for another 5 min. The temperature was cooled down to room temperature and a 15 mL mixture of toluene/methanol = 1:1 was added. The whole resulting product was centrifuged and washed three times with a 15 mL mixture of toluene/methanol = 1:1. The products were naturally dried in the glovebox.

Synthesis of single-layer WS_2 nanosheets: The single-layer WS_2 nanosheets were synthesized using the same method for MoS_2 nanosheets, except that $(NH_4)_2MoS_4$ was replaced by ammonium tetrathiotungstate [$(NH_4)_2WS_4$, 4 mmol].

Synthesis of single-layer ReS_2 nanosheets: The single-layer ReS_2 nanosheets were synthesized using the same method for MoS_2 nanosheets, except that $(NH_4)_2MoS_4$ was replaced by tetrabutylammonium tetrathiorhenate(VII) [$(C_4H_9)_4$-$NReS_4$, 0.1 mmol].

Synthesis of SnS_2 nanosheets: $(NH_4)_4Sn_2S_6$ was prepared according to a literature method.[37] In a typical synthesis, 0.1 mmol of $(NH_4)_4Sn_2S_6$ was mixed with 7 mL of oleylamine and 8 mL of ODE in a 50 mL three neck round bottom flask. The mixture was degassed at 110 °C for 30 min. Then the temperature was raised to 280 °C under N_2 flow, and kept at this temperature for another 5 min. The temperature was cooled down to room temperature and a 15 mL mixture of toluene/methanol = 1:1 was added. The whole resulting product was centrifuged and washed three times with a 15 mL mixture of toluene/methanol = 1:1. The products were naturally dried in the glovebox.

Synthesis of Cu_xS nanoplates: The Cu_xS nanoplates were synthesized using the same method for SnS_2 nanosheets, except that $(NH_4)_4Sn_2S_6$ was replaced by copper(I) thiocyanate [CuSCN, 0.1 mmol].

Materials characterization

XRD patterns were acquired using a X'per PRO (PANalytical) X-ray diffractometer (40 kV, 40 mA) with Cu Kα radiation (λ=1.5406 Å). UV-Vis absorption spectroscopy was carried out on a Perkin Elmer Lambda 35 UV/vis spectrometer. TEM images were taken using a JEOL 2100 transmission electron microscope at an acceleration voltage of 120 kV. HAADF-STEM, HRTEM and STEM-EDX images were obtained on a FEI Titan G2 80-200 high-resolution transmission electron microscope. AFM measurements were performed on a Bruker Dimension Icon atomic force microscope with a Bruker NCHVA probe. XPS data were collected on a Kratos Axis Ultra DLD spectrometer. The binding energy scale was calibrated for each sample by setting the main line of the C 1s spectrum to 284.8 eV. Each high-resolution spectrum was fitted with a Gaussian-Lorentzian (70%-30%) line shape using a Shirley background. Nuclear magnetic resonance (NMR) test was carried out at AVANCE 400 MHz (Bruker) using deuterated methanol with sample to solvent ratio of 3:4.

Solar H_2 fuel production

Photocatalytic hydrogen production from methanol was conducted in a 15 mL quartz bottle reactor with a silicone rubber septum under room temperature and atmospheric pressure. A 300 W commercial microsolar lamp (Beijing Perfect light Technology Co., Ltd) with an optical filter of AM 1.5 G was horizontally placed alongside the reactor. A certain amount of photocatalyst was loaded into the reactor while 90 min sonication was performed to dissolve the photocatalysts into the methanol solution. After that, the reactor was degassed for another 30 min to remove the residual air from the reactor by means of argon gases. The products from the photocatalytic methanol decomposition was analysed by GC which equipped with a TCD, and FID detectors and a chromatographic column. Before and after light irradiation, 50 μL of aliquots from the reactor dead space was taken out by a micro-syringe and manually injected into the GC (Nexis 2030, Shimadzu Scientific instruments), which will work as the reference. Typically, the photocatalytic reaction was carried out for 4 h, while the stability test

was done for 66 h per cycle. During our measurement and analysis on the H_2 generation, we did not extract out the first point of the generated H_2 amount, we normally analyze the generated H_2 amount every two hours or longer duration after the light illumination.

Computational methods

Calculations were performed at the density functional theory level by using the Vienna *Ab initio* Simulations Package (VASP)[28,38] and projected augmented wave (PAW) method[39-41] (with $1s^1$, $2s^22p^2$, $2s^22p^3$, $3s^23p^4$, $4d^55s^1$ as valence electrons for H, C, N, S and Mo, respectively). The exchange-correlation interaction was treated with different approximations including the local density approximation (LDA) and the generalized gradient approximation (GGA) parameterized by Perdew, Burke and Ernzerhof (PBE).[42] Van der Waals interaction was treated by employing the empirical correction of Grimme (DFT-D2).[43] The cutoff energy of plane-wave basis was set to 600 eV. Brillouin zone was sampled by using a Gamma-centred ***k***-point set of 13×13×1 for 1H-MoS_2 and similar dense k-mesh was used for other structures. The total energy was able to converge within 1 meV/atom. The energy was converged within 10^{-4} eV/cell and the force was converged to less than 0.01 eV/Å for all structure relaxations.

We firstly calculated the interlayer cohesion energy of MoS_2, from $E_{coh} = (E_{bulk} - nE_{single})/nA$, where E_{bulk} is the total energy of bulk MoS_2 (space group *R3m*, No. 160), E_{single} is the total energy of single-layer MoS_2, *n* is the number of layers in the bulk, and A is the area of basal plane per formula. The calculated E_{coh} by different methods are plotted in Figure 2b. Then, we investigated the adsorption of NH_3 and H_2S molecules on single-layer MoS_2 in a 2×2×1 supercell. The occupancy number is determined by the number of molecules (*N*) on one side of MoS_2 single-layer over the number of MoS_2 formulas (four) in the supercell. For each occupancy, we considered several configurations that are likely to happen. We calculated the adsorption energy for adsorbed molecules by

$E_{ads} = \left(E_{MoS_2} + N E_{molecule} - E_{(MoS_2+molecule)}\right)$, which can be converted to the cohesion energy between MoS_2 and molecules by $E_{coh} = E_{ads}/4A$.

Supporting Information

Supporting Information is available from the Wiley Online Library or from the author.

Acknowledgement

This work was supported by Australian Research Council (ARC) Discovery Early Career Researcher Award (DECRA) (DE 160100589), ACR Discovery Project (DP190100295), ARC LIEF scheme (LE190100014), the ANU Futures Scheme (Q4601024) and ANU Global Research Partnership Scheme (R468504649). Y. Li acknowledges support from the NSFC (grant no. 11674131). Y. Pang acknowledged the scholarship from the China Scholarship Council. M. N. Uddin acknowledged the Australian Government Research Training Program scholarship. The authors acknowledge Jean-Pierre Veder from the John de Laeter Research Centre for Microscopy, Characterization & Analysis Curtin University, Australia for technical assistance in XPS characterizations. The authors acknowledge the facilities, and the scientific and technical assistance of the Australian Microscopy & Microanalysis Research Facility at the Centre for Microscopy, Characterisation & Analysis, The University of Western Australia, a facility funded by the University, State and Commonwealth Governments. The authors acknowledge the assistance in the electron paramagnetic resonance (EPR) measurement from Dr Nick Cox's group, Research School of Chemistry, the Australian National University.

Received: ((will be filled in by the editorial staff))
Revised: ((will be filled in by the editorial staff))
Published online: ((will be filled in by the editorial staff))

Conflict of interest

The authors declare no competing interests.

Keywords

single-layer transition metal dichalcogenides, two-dimensional materials, methanol-storable H_2 fuel, solar-driven photocatalysis

References

[1] a) J. Mann, Q. Ma, P. M. Odenthal, M. Isarraraz, D. Le, E. Preciado, D. Barroso, K. Yamaguchi, G. von Son Palacio, A. Nguyen, T. Tran, M. Wurch, A. Nguyen, V. Klee, S. Bobek, D. Sun, T. F. Heinz, T. S. Rahman, R. Kawakami, L. Bartels, *Adv. Mater.* **2014**, *26*, 1399; b) X. Chen, A. R. McDonald, *Adv. Mater.* **2016**, *28*, 5738.

[2] a) D.-H. Kang, S. R. Pae, J. Shim, G. Yoo, J. Jeon, J. W. Leem, J. S. Yu, S. Lee, B. Shin, J.-H. Park, *Adv. Mater.* **2016**, *28*, 7799; b) Y. Zhang, B. Zheng, C. Zhu, X. Zhang, C. Tan, H. Li, B. Chen, J. Yang, J. Chen, Y. Huang, L. Wang, H. Zhang, *Adv. Mater.* **2015**, *27*, 5738.

[3] a) Q. Lu Y. Yu, Q. Ma, B. Chen, H. Zhang, *Adv. Mater.* **2016**, *28*, 1917; b) J. Zhang, S. Liu, H. Liang, R. Dong, X. Feng, *Adv. Mater.* **2015**, *27*, 7426.

[4] a) M. Nasilowski, B. Mahler, E. Lhuillier, S. Ithurria, B. Dubertret, *Chem. Rev.* **2016**, *116*, 10934; b) Y. Du, Z. Yin, J, Zhu, X. Huang, X.-J. Wu, Z. Zeng, Q. Yan, H. Zhang, *Nat. Commun.* **2012**, *3*, 1177; c) B. Mahler, V. Hoepfner, K. Liao, G. A. Ozin, *J. Am. Chem.Soc.* **2014**, *136*, 14121; d) Z. Liu, N. Li, C. Su, H. Zhao, L. Xu, Z. Yin, J. Li, Y. Du, *Nano Energy* **2018**, *50*, 176.

[5] D. Sun, S. Feng, M. Terrones, R. E. Schaak, *Chem. Mater.* **2015**, *27*, 3167.

[6] Y. Sun, Y. Wang, D. Sun, B. R. Carvalho, C. G. Read, C.-h. Lee, Z. Lin, K. Fujisawa, J. A. Robinson, V. H. Crespi, M. Terrones, R. E. Schaak, *Angew. Chem. Int. Ed.* **2016**, *55*, 2830.

[7] J. H. Han, S. Lee, J. Cheon, *Chem. Soc. Rev.* **2013**, *42*, 2581.

[8] J. H. Han, M. Kwak, Y. Kim, J. Cheon, *Chem. Rev.* **2018**, *118*, 6151.

[9] C. Tan, X. Cao, X.-J. Wu, Q. He, J. Yang, X. Zhang, J. Chen, W. Zhao, S. Han, G.-H. Nam, M. Sindoro, H, Zhang, *Chem. Rev.* **2017**, *117*, 6225.

[10] E. Lhuillier, S. Pedetti, S. Ithurria, B. Nadal, H. Heuclin, B. Dubertret, *Acc. Chem. Res.*

2015, *48*, 22.

[11] Y. Pang, M. Zhang, D. Chen, W. Chen, F. Wang, S. Javaid, M. Saunders, M. R. Rowles, L. Liu, S. Liu, A. Sitt, C. Li, G. Jia, *J. Phys. Chem. Lett.* **2019**, *10*, 3465.

[12] C. Schliehe, B. H. Juarez, M. Pelletier, S. Jander, D. Greshnykh, M. Nagel, A. Meyer, S. Foerster, A. Kornowski, C. Klinke, H. Weller, *Science* **2010**, *329*, 550.

[13] Z. Liu, Z. Yin, C. Cox, M. Bosman, X. Qian, N. Li, H. Zhao, Y. Du, J. Li, D. G. Nocera, *Sci. Adv.* **2016**, *2*, e1501425.

[14] M. Nielsen, E. Alberico, W. Baumann, H.-J. Drexler, H. Junge, S. Gladiali, M. Beller, *Nature* **2013**, *495*, 85.

[15] W. Cui, C. Xu, S. Zhang, L. Feng, S. Lü, F. Qiu, *J. Photochem. Photobiol. A: Chem.* **2005**, *175*, 89.

[16] C. Altavilla, M. Sarno, P. Ciambelli, *Chem. Mater.* **2011**, *23*, 3879.

[17] T. Böker, R. Severin, A. Müller, C. Janowitz, R. Manzke, D. Voß, P. Krüger, A. Mazur, J. Pollmann, *Phys. Rev. B* **2005**, *64*, 235305.

[18] a) M. Zhou, Z. Zhang, K. Huang, Z. Shi, R. Xie, W. Yang, *Nanoscale* **2016**, *8*, 15262; b) G. Jia, A. Sitt, G. B. Hitin, I. Hadar, Y. Bekenstein, Y. Amit, I. Popov, U. Banin, *Nat. Mater.* **2014**, *13*, 301; c) G. Jia, U. Banin, *J. Am. Chem. Soc.* **2014**, *136*, 11121.

[19] W. Jung, S. Lee, D. Yoo, S. Jeong, P. Miró, A. Kuc, T. Heine, J. Cheon, *J. Am. Chem. Soc.* **2015**, *137*, 7266.

[20] G. Guan, S. Zhang, S. Liu, Y. Cai, M. Low, C. P. Teng, I. Y. Phang, Y. Cheng, K. L. Duei, B. M. Srinivasan, Y. Zheng, Y.-W. Zhang, M.-Y. Han, *J. Am. Chem. Soc.* **2015**, *137*, 6152.

[21] Y. Yin, J. Han, Y. Zhang, X. Zhang, P. Xu, Q. Yuan, L. Samad, X. Wang, Y. Wang, Z. Zhang, P. Zhang, X. Cao, B. Song, S. Jin, *J. Am. Chem. Soc.* **2016**, *138*, 7965.

[22] Y. Liu, Y.-X. Yu, W.-D. Zhang, *J. Phys. Chem. C* **2013**, *117*, 12949.

[23] T. Weber, J. C. Muijsers, J. H. M. C. van Wolput, C. P. J. Verhagen, J. W. Niemantsverdriet, *J. Phys. Chem.* **1996**, *100*, 14144.

[24] T.P. Prasad, E. Diemann, A. Müller, *J. Inorg. Nucl. Chem.* 1973, *35*, 1895.

[25] Y. Li, Y.-L. Li, B. Sa, R. Ahuja, *Catal. Sci. Technol.* **2017**, *27*, 545.

[26] S. Zhao, J. Xue, W. Kang, *Chem. Phys. Lett.* **2014**, *595−596*, 35.

[27] Z. Yin, H. Li, H. Li, L. Jiang, Y. Shi, Y. Sun, G. Lu, Q. Zhang, X. Chen, H. Zhang, *ACS Nano* **2011**, *6*, 74.

[28] C. Tsai, F. Abild-Pedersen, J. K. Nørskov, *Nano Lett.* **2014**, *14*, 1381.

[29] T. F. Jaramillo, K. P. Jørgensen, J. Bonde, J. H. Nielsen, S. Horch, I. Chorkendorff,

Science **2007**, *317*, 100.

[30] Y.-Y. Chen, M. Dong, Z. Qin, X.-D. Wen, W. Fan, J. Wang, *J. Mol. Catal. A: Chem.* **2011**, *338*, 44.

[31] B. Hinnemann, P. G. Moses, J. Bonde, K. P. Jørgensen, J. H. Nielsen, S. Horch, I. Chorkendorff, J. K. Nørskov, *J. Am. Chem. Soc.* **2005**, *127*, 5308.

[32] P.-Y. Prodhomme, P. Raybaud, H. Toulhoat, *J. Catal.* **2011**, *280*, 178.

[33] S. Kandoi, J. Greeley, M. A. Sanchez-Castillo, S. T. Evans, A. A. Gokhale, J. A. Dumesic, M. Mavrikakis, *Top. Catal.* **2006**, *37*, 17.

[34] H. Wang, H. Yuan, S. S. Hong, Y. Li, Y. Cui, *Chem. Soc. Rev.* **2015**, *44*, 2664.

[35] H. Zeng, X. Cui, *Chem. Soc. Rev.* **2015**, *44*, 2629.

[36] A. Castellanos-Gomez, H. S. van der Zant, G. A. Steele, *Nano Res.* **2014**, *7*, 572.

[37] M. V. Kovalenko, M. I. Bodnarchuk, J. Zaumseil, J.-S. Lee, D. V. Talapin, *J. Am. Chem. Soc.* **2010**, *132*, 10085.

[38] a) G. Kresse, D. Joubert, *Phys. Rev. B* **1999**, *59*, 1758; b) P. E. Blöchl, *Phys. Rev. B* **1994**, *50*, 17953.

[39] G. Kresse, J. Furthmüller, *Comput. Mater. Sci.* **1996**, *6*, 15.

[40] G. Kresse, J. Furthmüller, *Phys. Rev. B* **1996**, *54*, 11169.

[41] G. Kresse, J. Hafner, *Phys. Rev. B* **1993**, *48*, 13115.

[42] J. P. Perdew, K. Burke, M. Ernzerhof, *Phys. Rev. Lett.* **1996**, *77*, 3865.

[43] S. Grimme, *J. Comput. Chem.* **2006**, *27*, 1787.

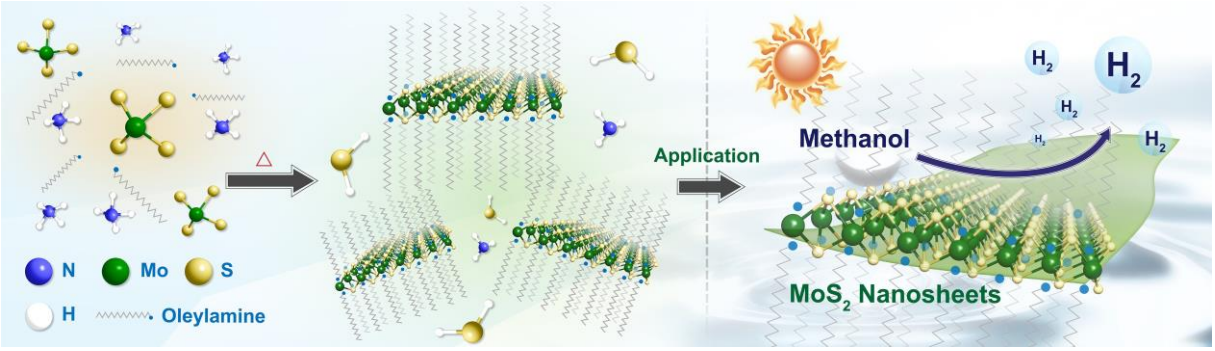

Scheme 1. Synthetic and methanol photocatalytic application of single-layer MoS_2 nanosheets.

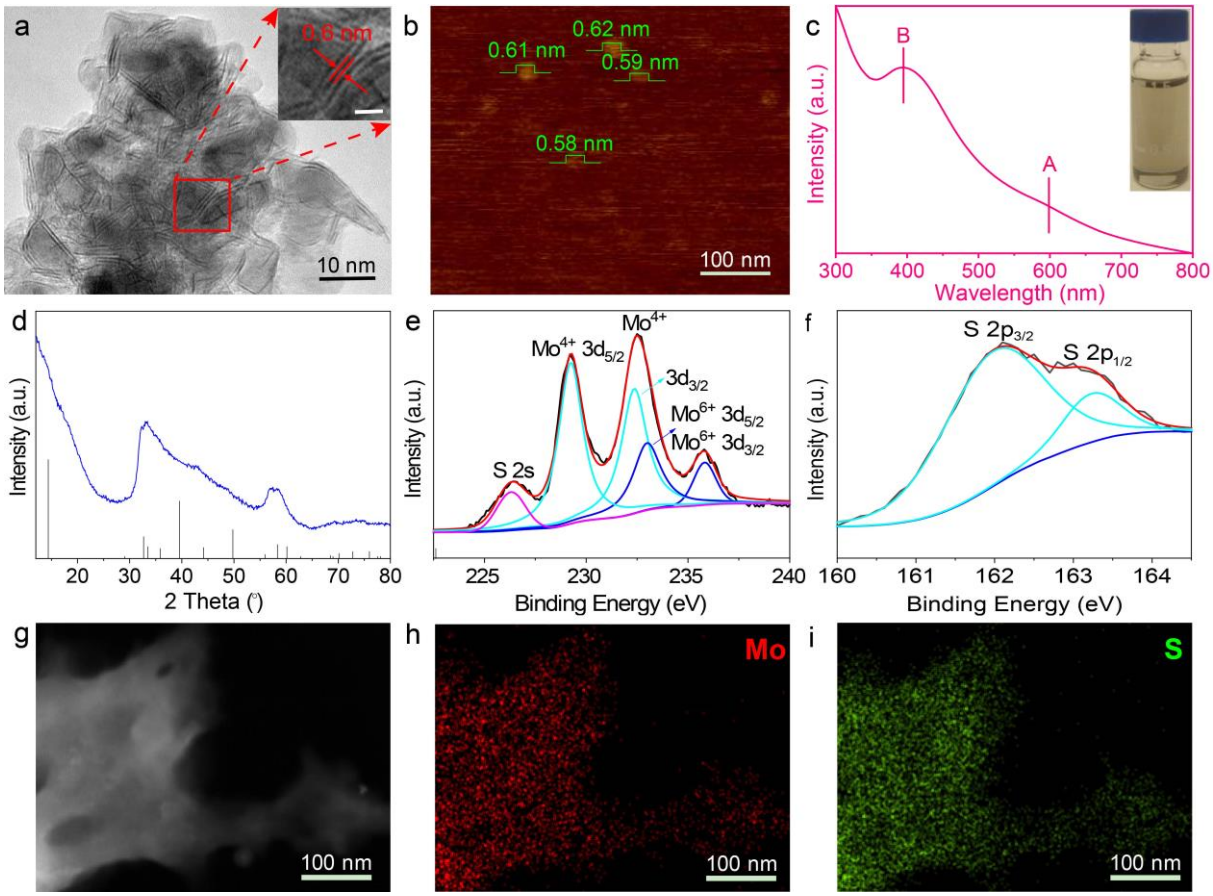

Figure 1. Characterizations of single-layer MoS_2 nanosheets. a, TEM image of single-layer MoS_2 nanosheets. Inset shows the thickness of 0.6 nm of MoS_2 nanosheets standing on their edges. Scale bar: 2 nm. **b,** AFM image shows the thickness of several individual single-layer MoS_2 nanosheets. **c,** UV-Vis absorption spectrum of single-layer MoS_2 nanosheets. Inset: Photograph of as-synthesized MoS_2 nanosheets dissolved in chloroform. **d,** XRD pattern of single-layer MoS_2 nanosheets assembled on a Si wafer. **e,f,** XPS spectra of (e) Mo_{3d}, and (f) S_{2p} of MoS_2 nanosheets. **g,** HAADF-STEM image of MoS_2 nanosheets. **h,i,** STEM-EDS elemental mapping of (h) Mo and (i) S of as-synthesized MoS_2 nanosheets.

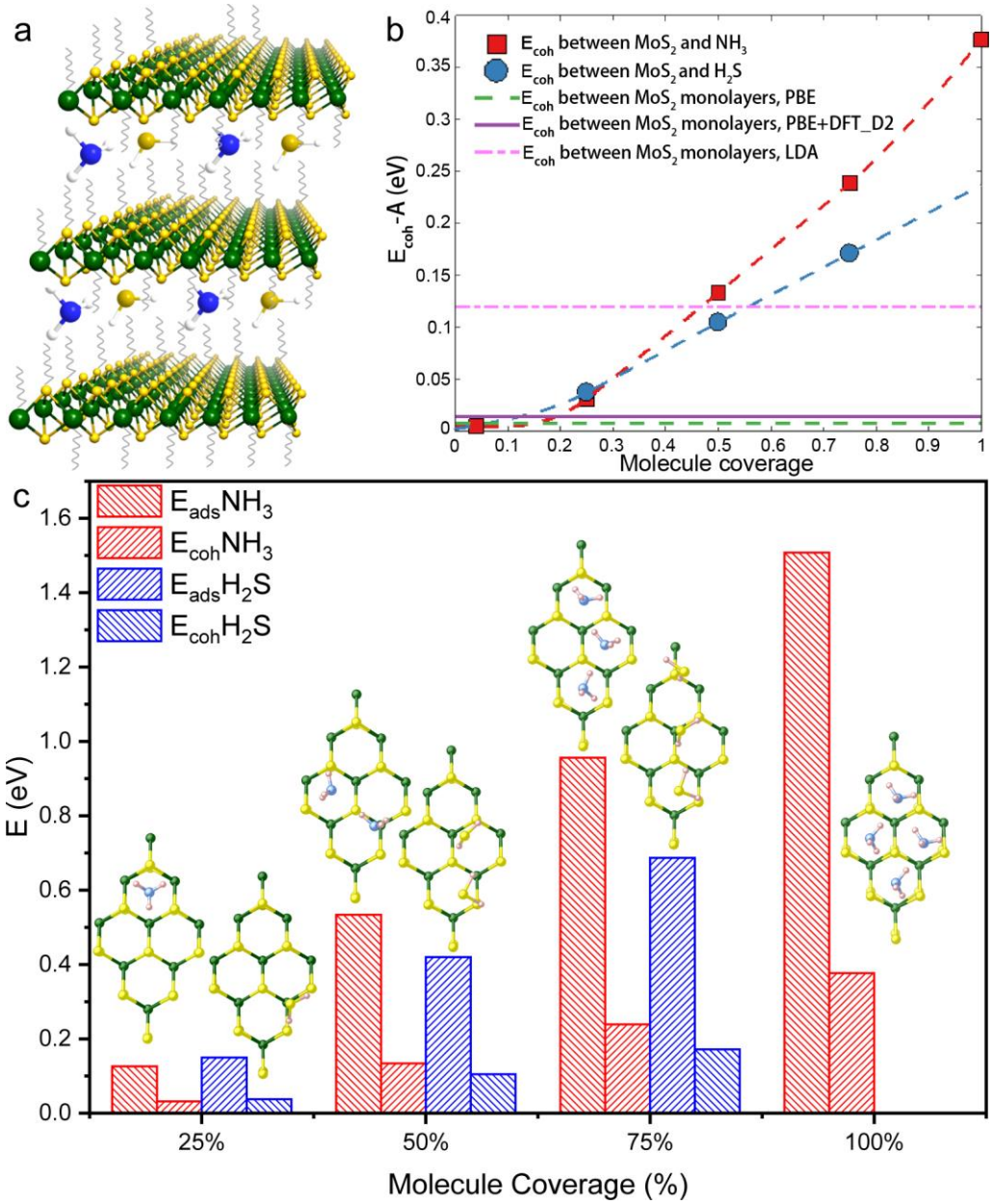

Figure 2. Growth mechanism of single-layer MoS_2 nanosheets. a, Three-dimensional representation of NH_3 and H_2S molecular intercalated between 3-layer MoS_2 nanosheets. **b,** Interlayer cohesion energy (E_{coh}) in bulk MoS_2 (*R3m*) and between single-layer MoS_2 nanosheets and molecules. A is the area of basal plane. Data at 4% is from.[14] **c,** The converted cohesion energy (E_{coh}) and the adsorption energy (E_{ads}) for NH_3 and H_2S on basal plane of single-layer MoS_2 nanosheets with different molecule coverage. Inset: Configurations of NH_3 and H_2S molecules adsorbed on single-layer MoS_2 nanosheets. Mo, S, N and H are represented by green, yellow, blue and pink balls, respectively.

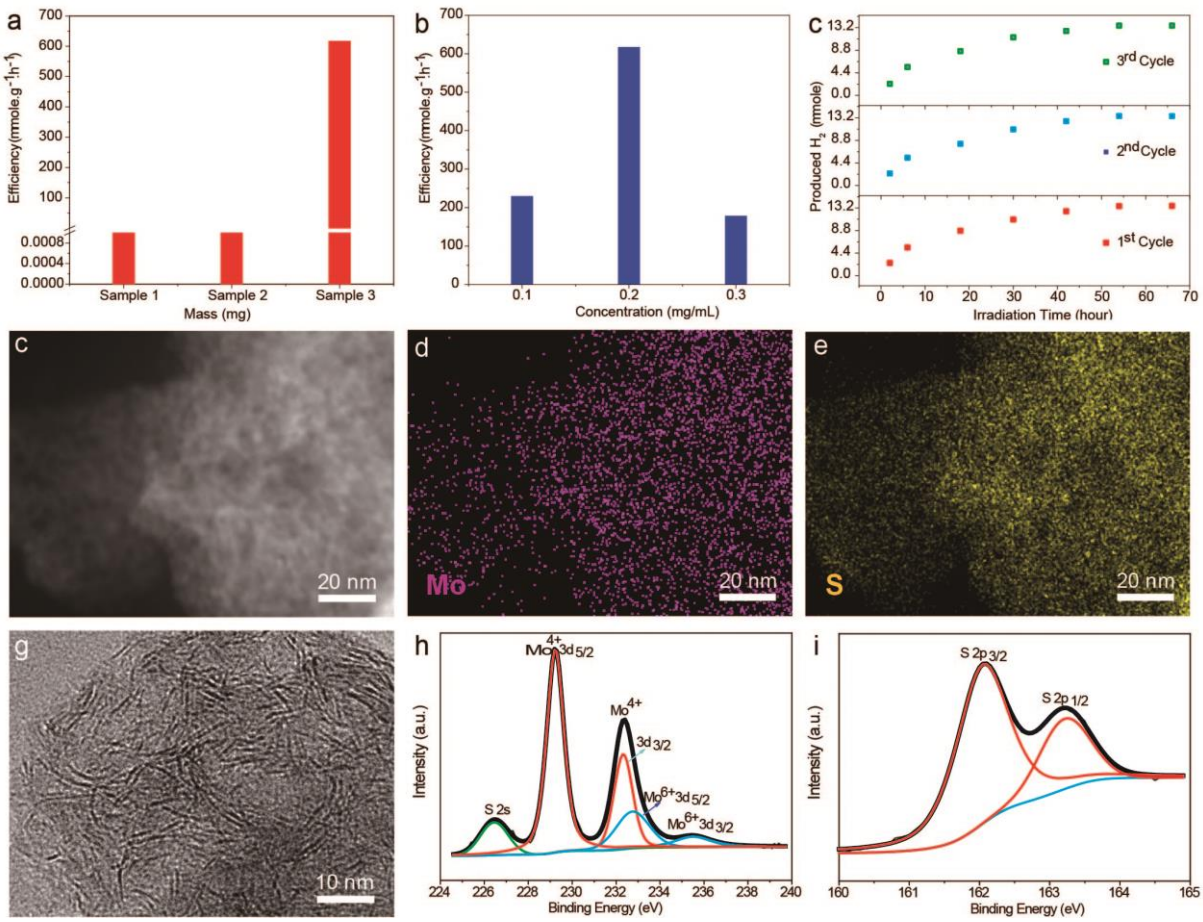

Figure 3. Photocatalytic performances and characterizations of single-layer MoS_2 nanosheets after photocatalysis cycling. a, Effects of surfactant, methanol and photocatalysts on MTH efficiency between three different samples while keeping all other experimental conditions the same. Sample 1: 10 mL (~ 8.2 $\times 10^3$ mg) pure surfactant, sample 2: 5 mL surfactant + 5 mL methanol, and sample 3: 2 mg MoS_2 in 10 mL methanol. **b,** Concentration profile of MoS_2 for H_2 production rate. **c,** Absolute H_2 yield after 3 consecutive cycling photocatalytic test of single-layer MoS_2 nanosheets. **d,** STEM image of MoS_2 nanosheets after photocatalysis cycling. **e,f,** STEM-EDS elemental mapping of (e) Mo and (f) S of as-synthesized MoS_2 nanosheets after photocatalysis cycling. **g,** The high-magnification TEM image of MoS_2 nanosheets after photocatalysis cycling. **h,i,** X-ray photoelectron spectroscopy (XPS) spectra of (h) Mo_{3d}, and (i) S_{2p} of MoS_2 nanosheets after photocatalysis cycling.

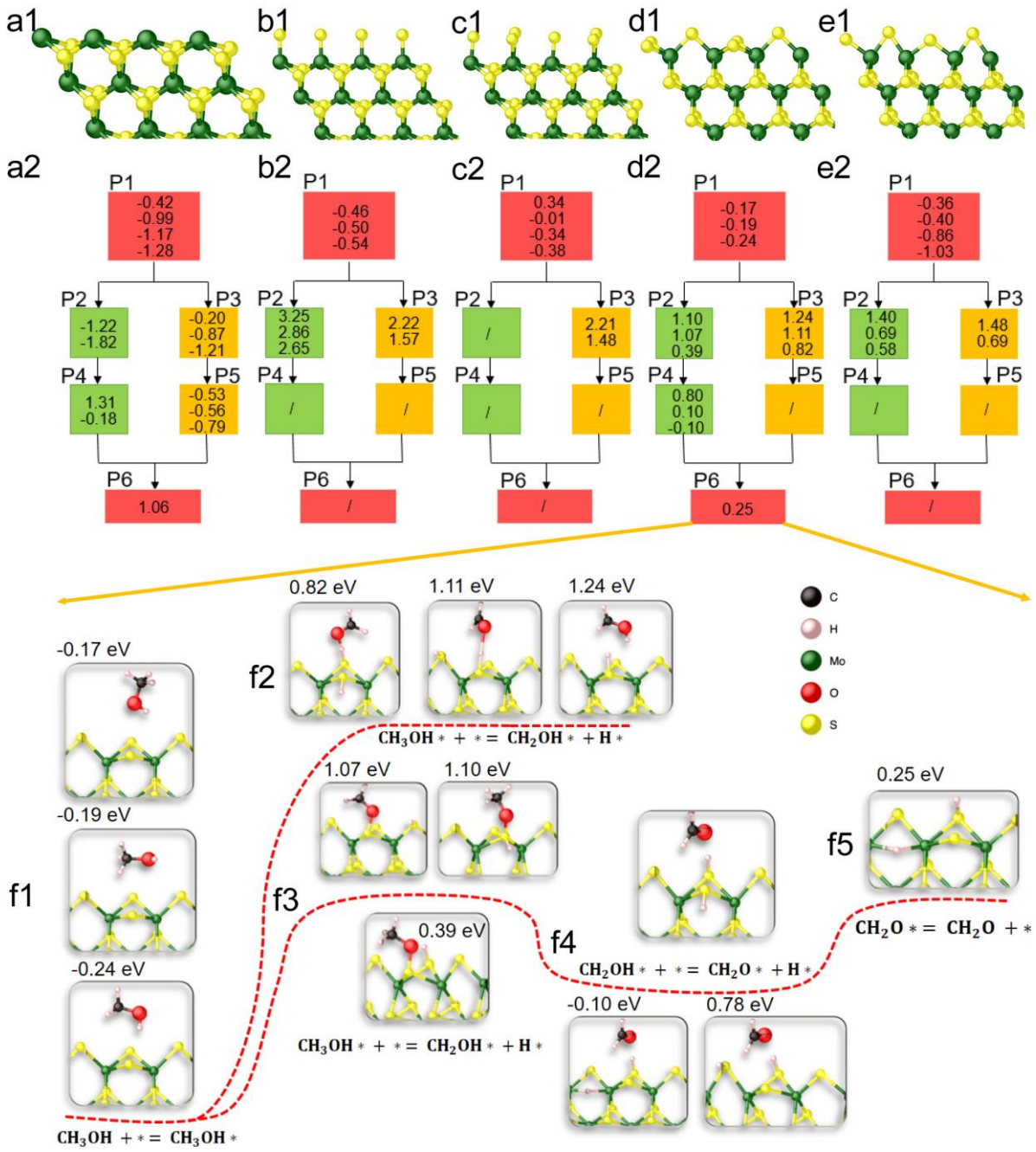

Figure 4. DFT calculations. a1-e1, Relaxed edge structures for (a1) Mo-edge-b, (b1) Mo-edge-m, (c1) Mo-edge-m+d, (d1) S-edge-m+d, and (e1) S-edge-m edges, respectively. Mo and S are represented by green and yellow balls, respectively. **a2-e2,** Free energies ΔG (in eV) for elementary reaction processes of hydrogen evolution from methanol catalysed on (a2) Mo-edge-b, (b2) Mo-edge-m, (c2) Mo-edge-m+d, (d2) S-edge-m+d, and (e2) S-edge-m edges, respectively. P1 to P6 are the elementary processes. Numbers inside box are ΔG and the

number in bold text indicates the lowest one. We stopped exploring further reactions if the lowest ΔG is bigger than 0.5 eV. The free energy for P2 in (c2) was not calculated because there is no stable site available to locate H from the O-H bond scission. **f1-f5,** Configurations of adsorbed specifieson the S-edge-m+d edge. (f1) CH_3OH molecule, (f2) CH_3O*+H $*$, (f3) CH_2O*+ $*$, (f4) $CH_2OH* + *$, and (f5) CH_2O*.

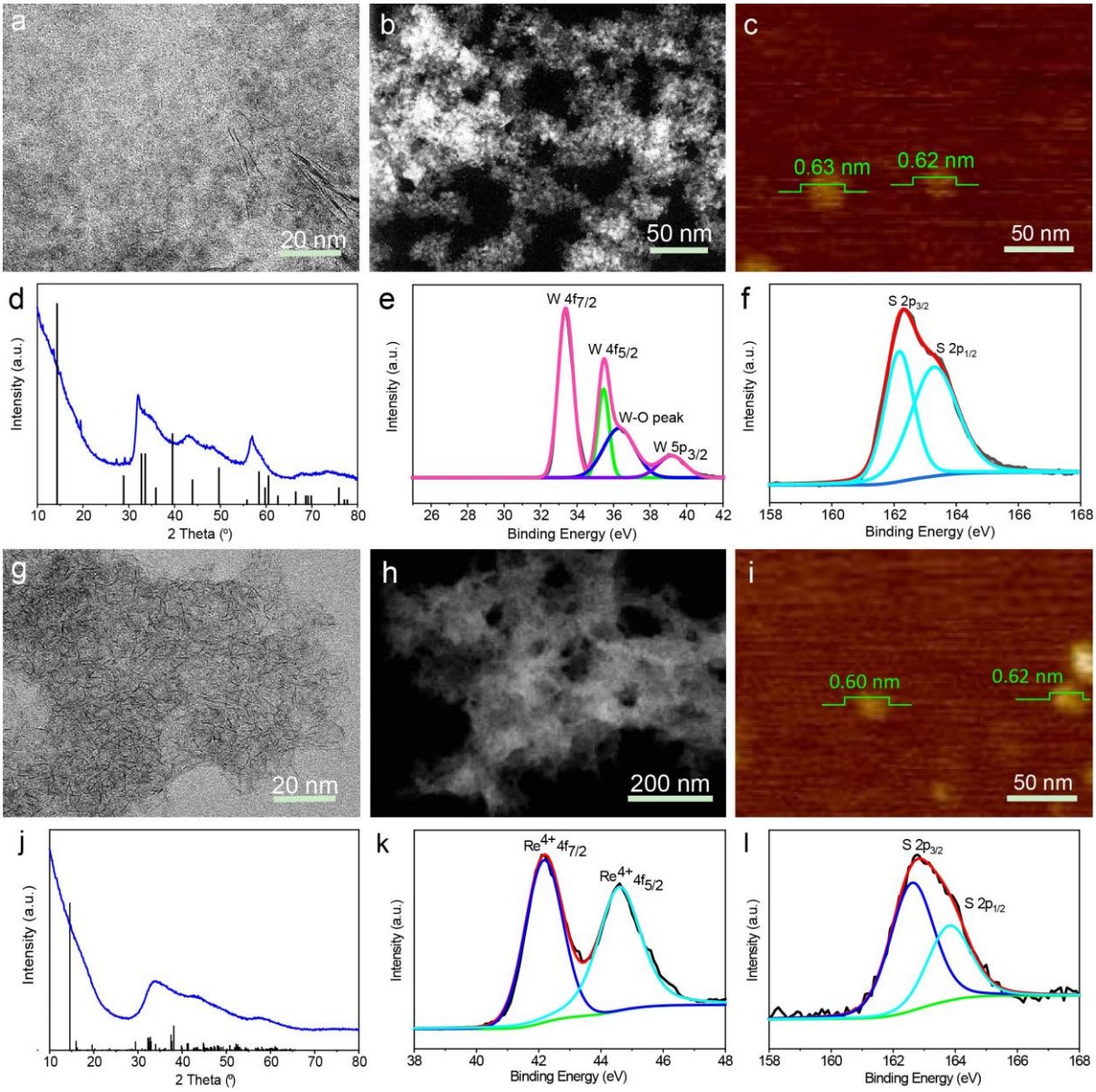

Figure 5. Characterizations of single-layer WS_2 and ReS_2 nanosheets. a, TEM image of WS_2 nanosheets. **b,** STEM image of WS_2 nanosheets. **c,** AFM image shows the thickness of a single-layer WS_2 nanosheet. **d,** XRD pattern of WS_2 nanosheets assembled on a Si wafer. **e,f,** XPS spectra of (e) W_{4f}, and (f) S_{2p} of WS_2 nanosheets. **g,** TEM image of ReS_2 nanosheets. **h,** STEM image of ReS_2 nanosheets. **i,** AFM image showing the thickness of a single-layer ReS_2 nanosheet. **j,** XRD pattern of ReS_2 nanosheets assembled on a Si wafer. **k,l,** XPS spectra of (k) Re_{4f}, and (l) S_{2p} of ReS_2 nanosheets.

The table of contents: A scalable stacking-hinderable strategy has been developed to enable exclusive single-layer growth mode for transition metal dichalcogenides selectively sandwiched by surfactant molecules, which can act as efficient solar-driven photocatalysts for solar H_2 fuel production from hydrogen-stored liquid carrier–methanol.

Keywords: single-layer transition metal dichalcogenides, two-dimensional materials, methanol-storable H_2 fuel, solar-driven photocatalysis

Colloidal Single-Layer Photocatalysts for Methanol-Storable Solar H_2 Fuel

Yingping Pang,[†] Md Nasir Uddin,[†] Wei Chen, Shaghraf Javaid, Emily Barker, Yunguo Li,[*] Alexandra Suvorova, Martin Saunders, Zongyou Yin,[*] and Guohua Jia[*]

ToC figure